CrystEngComm

ROYAL SOCIETY OF CHEMISTRY

PAPER

View Article Online
View Journal | View Issue

Cite this: *CrystEngComm*, 2024, **26**, 4146

Structure and electrical properties of Cu, Bi and Mn co-doped $K_{0.5}Na_{0.5}NbO_3$ single crystals grown by the seed-free solid state crystal growth method

Yuan Xu,[a] Minhong Jiang, *[ab] Xinkang Liu,[a] Yujiao Zeng,[a] Shixuan Cao,[a] Yujiao Ouyang,[a] Jianwei Song[a] and Guanghui Rao*[a]

Received 18th May 2024,
Accepted 1st July 2024

DOI: 10.1039/d4ce00502c

rsc.li/crystengcomm

$K_{0.5}Na_{0.5}NbO_3$ (KNN) crystals have great application prospects due to their excellent piezoelectric properties, high Curie temperature, and environmental friendliness. Currently, KNN crystals grown by the seed-free solid-state crystal growth (SFSSCG) method exhibit relatively high dielectric loss. In order to reduce their dielectric loss, Cu, Bi and Mn co-doped KNN lead-free piezoelectric single crystals were prepared by the SFSSCG method. The effects of the CuO doping content on the structure and electrical properties of $(1 - x)(0.996KNN–0.004BiMnO_3)–xCuO$ crystals were systematically studied. The results show that an appropriate doping amount of CuO is beneficial for the growth of the crystals and the improvement of electrical properties. When the diameter of the billets is 40 mm, the maximum crystal size of 25 × 21 × 2 mm^3 is obtained. All crystals have a typical perovskite structure almost with a single orthorhombic phase and are very compact almost without holes. The minimum average domain width of 276 nm is obtained for the crystal at x = 0.005. The KNN crystals exhibit normal ferroelectric characteristics and a space-charge-limited-conduction (SCLC) mechanism. The introduction of Cu^{2+} ions reduces the dielectric loss of the crystal and increases its piezoelectric and dielectric properties. The Cu, Bi and Mn co-doped KNN crystals achieve excellent comprehensive properties: d_{33} = 314 pC N^{-1}, P_r = 29.9 μC cm^{-2}, E_c = 10.1 kV cm^{-1}, d^*_{33} = 869 pm V^{-1}, Q_m = 56.8, K_t = 0.38, $\tan\delta$ = 0.013 and T_C = 409 °C. This provides a route to improve the electrical properties of KNN-based crystals.

Introduction

Piezoelectric materials are widely used in the fields of electronic information due to their high output power, high precision and stability, such as in acoustic sensors, infinite communication, medical imaging, *etc.*[1–3] Usually, lead-containing piezoelectric materials show outstanding performance, but with the increasing awareness of environmental protection, it is very urgent to develop environmentally friendly and non-toxic lead-free piezoelectric materials. Potassium sodium niobate (KNN)-based piezoelectric materials are considered to be one of the most likely systems to replace lead-containing piezoelectric materials owing to their excellent piezoelectric properties, environmental friendliness, high Curie temperature, mechanical quality factors, *etc.*[4–13]

Piezoelectric single crystals and ceramics are common piezoelectric materials, but in the same composition, piezoelectric single crystals generally exhibit higher piezoelectric properties than ceramics made of polycrystalline particles. For example, the piezoelectric coefficient (d_{33}) of normal $Na_{0.5}Bi_{0.5}TiO_3–BaTiO_3$ ceramics is about 100–150 pC N^{-1},[14,15] but $Na_{0.5}Bi_{0.5}TiO_3–BaTiO_3$ single crystals show a higher piezoelectric coefficient. KNN-based piezoelectric materials would also exhibit such characteristics. It was reported that the d_{33} value of KNN-based single crystals reached 1050 pC N^{-1},[13] which was about 6 times that of normal KNN-based ceramics. At present, single crystals have been normally prepared by traditional melt growth or solution growth methods, such as top-seeded solution growth (TSSG), floating zone melting (FZ), flux and hydrothermal methods and so on. Among them, the TSSG method is considered to be one of the most effective techniques for growing large KNN single crystals.[16] For example, Huo *et al.* prepared KNN single crystals with a piezoelectric coefficient (d_{33}) of 255 pC N^{-1} by the TSSG method.[17] The d_{33} of $(K_{0.44}Na_{0.46})NbO_3–0.5\%MnO_2$ single crystals prepared by Zhou *et al.* using the TSSG method reached 261 pC N^{-1},[18] and the dimensions of KNN single

[a] *Guangxi Key Laboratory of Information Materials, School of Material Science and Engineering, Guilin University of Electronic Technology, GuangxiGuilin 541004, China. E-mail: jiangmh@guet.edu.cn, rgh@guet.edu.cn*
[b] *Engineering Research Center of Electronic Information Materials and Devices, Ministry of Education, Guilin University of Electronic Technology, Guilin 541004, China*

crystals prepared by Deng *et al.* using the same method reached Ø30 × 10 mm.[19] However, these methods have many limitations: such as high energy consumption, complex processes and high cost, so people are actively looking for new methods to prepare KNN single crystals. Recently, our group developed a seed-free, solid-state crystal growth (SFSSCG) method to grow KNN-based crystals.[20–27] At temperature below the melting temperature of the system, centimeter-scale bulk KNN single crystals with a low segregation coefficient can be grown by a simple route similar to the ceramic process. Compared with the above traditional methods, the SFSSCG method has extraordinary advantages such as low energy consumption, low investment, high composition uniformity, *etc.*, and can overcome the problems of incompatible melting and high volatility. By this SFSSCG method, Jiang *et al.* have successfully prepared a series of bulk KNN-based single crystals.[5–12] Subsequently, Yang[28] and Ahn[3] *et al.* also obtained KNN-based crystals by the similar method.

Currently, KNN-based crystals grown by the SFSSCG method still have some problems, such as non-sufficient size, relatively high dielectric loss, numerous microdefects, *etc.* Based on our previous exploration of the SFSSCG method, the addition of trace Bi elements plays an important role in the growth of KNN single crystals,[5–13] but the existence of Bi may also be one of the main reasons for high dielectric loss and numerous microdefects in the crystals. Research studies show that doping is an effective way to improve the electrical properties of the KNN system. Peng *et al.* found that KNN ceramics doped with $Bi_{0.5}Li_{0.5}ZrO_3$ exhibited higher d_{33}, K_p and P_r than undoped KNN ceramics.[29] Meanwhile, the addition of the Mn element has been proved to be able to effectively suppress the leakage current and space charge polarization, thus improving the piezoelectric, ferroelectric and dielectric properties of the KNN system. Wang *et al.* reported that introduction of Mn in Bi-containing KNN-based crystals enhanced their electrical properties.[5] Usually, CuO doping has been also used to reduce the dielectric loss of KNN-based ceramics while improving their mechanical quality factor.[30,31] Shen *et al.* found that compared with pure LT-KNN ceramics (Q_m = 69), the Q_m of LT-KNN + 1 mol% CuO ceramics was increased by nearly five times (Q_m = 323).[32] Zhou *et al.* found that CuO doping can improve the compactness of KNN-based ceramics.[33] Liu[34] and Yao[9] *et al.* found that an appropriate amount of CuO doping had a significant effect on the dielectric loss reduction of KNN single crystals, and the dielectric loss reached 1%.

In this study, Cu is used as the main dopant together with Bi and Mn elements to decrease the dielectric loss of KNN crystals and improve their piezoelectric properties. Lead-free piezoelectric $(1 - x)(0.996\text{KNN}–0.004\text{BiMnO}_3)–x\text{CuO}$ (x = 0–0.009) single crystals were prepared by the SFSSCG method. The effects of CuO doping on the growth, structure and electrical properties of the single crystals were systematically studied.

Experimental procedure

Single crystals of $(1 - x)(0.996K_{0.5}Na_{0.5}NbO_3–0.004BiMnO_3)–x\text{CuO}$ ($(1 - x)$(KNN-BM)–xCuO) [x = 0–0.009, according to the value of x, the samples were sequentially labeled CuO0, CuO0.1, CuO0.3, CuO0.5, CuO0.7, and CuO0.9] were prepared by the SFSSCG method. Reagent-grade Na_2CO_3 (>99.8%), K_2CO_3 (>99%), CuO (>99%), MnO_2 (>85.0%), and Bi_2O_3 (>99%) and Nb_2O_5 (>99.5%) powders were used as the raw materials. After baking at 120 °C for 2 hours, the raw material powders were ball milled in a specific plastic bottle with alcohol and zirconium balls for 24 hours, and then dried and calcined at 750 °C for 6 h in air. The mixture powders were sieved through a 150 mesh sieve to obtain powders with a grain size ≤106 μm. These fine powders were, thereafter, pressed into discs with a diameter of 25 mm and a thickness of 2–3 mm under a pressure of 100 MPa. Finally, these discs were sintered at 1110 °C for 21 hours in a muffle furnace. The single crystals were ground into single crystal wafers with a thickness of 0.5–0.6 mm through 800 mesh sandpaper. After being covered with silver paste on both sides, the wafers were polarized at 30 kV cm^{-1} in silicone oil for 30 min at 100 °C.

The crystalline structures were analyzed using an X-ray diffractometer (XRD; Empyrean PIXcel 3D, PANalytical, The Netherlands) with a 2θ angle of 20–80° and Cu-Kα radiation. The natural surfaces and domain structure of the single crystals were analyzed by field emission scanning electron microscopy (SEM; Quanta 450 FEG, FEI, USA). The chemical composition and distribution in the crystals were determined using an energy dispersive spectrometer (EDS; X-Max 20, Oxford Instruments, UK). Polarization–electrical field (P–E) loops at 10 Hz and unipolar strain–electrical field (S–E) loops at 20 kV cm^{-1} were measured at room temperature using a ferroelectric comprehensive analyzer (TF ANALYZER 2000HS, aixACCT Systems GmbH, Germany). Eventually, the samples after polarization were aged for 48 hours, and then their piezoelectric constant (d_{33}) was recorded by using a quasi-static d_{33} meter (ZJ-3AN, Institute of Acoustics, Academy of Sciences, China). The dielectric constant (ε_r)–temperature and dielectric loss ($\tan\delta$)–temperature relationships were measured using a precision impedance analyzer (HP4294A, ANGILENT, USA).

Results and discussion

Fig. 1 shows the photos of all the CuO-doped KNN-BM single-crystal samples prepared by the SFSSCG method. It

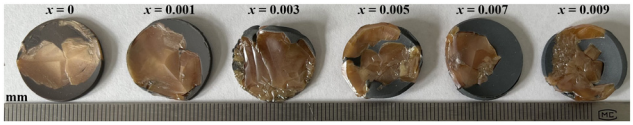

Fig. 1 Photos of $(1 - x)(0.996\ K_{0.5}Na_{0.5}NbO_3–0.004BiMnO_3)–x\text{CuO}$ (x = 0, 0.001, 0.003, 0.005, 0.007, 0.009) samples.

can be clearly found that a few bulk single crystals with obvious size were grown for all the samples, and the sample $(1 - x)$(KNN-MB)–xCuO (x = 0.003) obtained a single crystal with a maximum value of about 19 × 17 × 2 mm^3. These results show that an appropriate amount of CuO-doping is beneficial for the growth of KNN-based crystals. Additionally, the color of the single crystals gradually becomes darker by introducing Cu^{2+} dopants into the KNN lattices, which changes the photorefractive sensitivity and electron energy level required for charge transport in the crystals; the color of the crystals is related to the specific wavelength of light absorbed, since the absorption coefficient will increase with the increase of doping concentration, which will lead to a deeper color of the single crystal.[35] Fig. 2(a and b) show the single crystals grown under the conditions of two different diameters of green bodies. It can be seen that when the diameter is 40 mm, the maximum size of the single crystals reaches 25 × 21 × 2 mm^3, and when the diameter is 25 mm, the single crystals are smaller. This indicates that an appropriate increase in the diameter of the green body contributes to the further growth of the single crystals. The larger the diameter of the green bodies, the more nutrients and space provided for crystal growth, thus accelerating the crystal growth.

Fig. 3 shows the powder XRD patterns of the CuO-doped KNN-BM single crystals. It can be seen from Fig. 3(a) that all these single crystals have a typical perovskite structure with an orthorhombic phase. No diffraction patterns of any impurity phases are found in the XRD patterns, indicating that Cu^{2+} ions have completely entered the crystalline lattices and formed a stable solid solution. The XRD patterns of the crystals do not change significantly with increasing CuO content, indicating that the addition of CuO does not alter the perovskite crystalline structure of the crystals. Fig. 3(b) shows a local magnification of the XRD patterns in the 2θ range of 44–48°. It can be clearly seen that all single crystal samples have two main diffraction peaks in the range of 44–48°. The shape and position of the two peaks vary slightly with the CuO content, indicating a tiny lattice distortion induced by the CuO addition. The tiny lattice distortion can be attributed to the fact that since the radius of Cu^{2+} (0.073 nm) ions is close to that of Nb^{5+} (0.064 nm) ions at the B sites, like Mn^{3+} (0.058 nm) and Mn^{4+} (0.053 nm) ions, and far smaller than that of K^+ (0.151 nm) and Na^+ (0.102 nm) ions at the A site, Cu^{2+} ions preferentially occupy the B sites, which would only cause a slight lattice distortion without causing phase transition in the crystals.[13,36] Fig. 3(c–h) and Table 1 show the refinement results of XRD patterns (using the FullProf software). The refinements manifest that all the single-crystal samples show a two-phase coexisting crystal structure. However, according to the calculation results, the content of the tetragonal phase in the crystals is extremely low. Considering the possible errors in the refinements, the presence of the tetragonal phase in the crystals can be ignored. Furthermore, the unit cell parameters of the crystal samples doped with copper are close to those of the undoped samples, indicating that Cu^{2+} ions have entered the lattices of the system and formed a solid solution. These are consistent with the XRD patterns shown in Fig. 3(a) and (b).

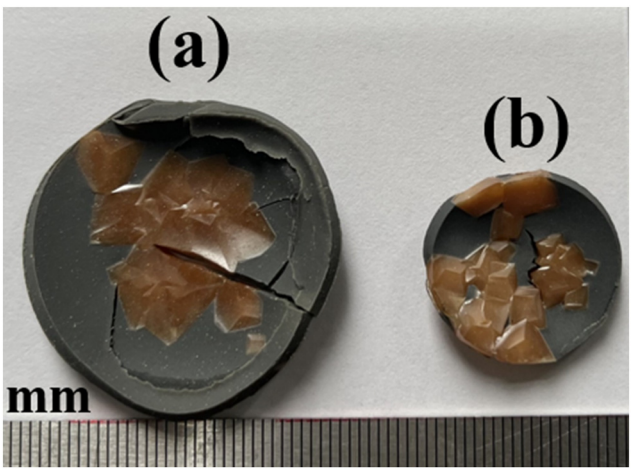

Fig. 2 Photos of (0.995)(0.996$K_{0.5}Na_{0.5}NbO_3$–0.004$BiMnO_3$)–0.005CuO under the conditions of green bodies with different diameters. (a) 40 mm and (b) 25 mm.

Fig. 4(a–f) show the exposed-superficial microstructure of the single crystal samples doped with different contents of CuO by SEM. It can be found that the exposed surface of the crystal without CuO-doping is relatively smooth and very compact with small parallel strip growth traces. After increasing the CuO-doping amount, as a whole the stripes become thicker with numerous and evenly distributed outcrops in the exposed surface of the crystal, indicating the promoting effect of CuO-doping on the crystal growth. All the crystal samples are very compact almost without holes. In addition, the layered-appearance structure indicates that the crystals grow in a two-dimensional layered manner, which is consistent with the two-dimensional growth mechanism.[22,37]

To understand the interior microstructure of the crystals and compare it with the external structure, these crystal samples were ultrasonically cleaned and then corroded. In fact, the samples were not subjected to polarization treatment before corrosion. Therefore, the original domain structure was maintained in the as-grown samples. The cross-section SEM micrographs of these crystals corroded after chemical etching with HF acid for 120 s are presented in Fig. 5. Due to the presence of positive and negative electrodes in ferroelectric materials, the corrosion efficiency of HF acid on these two electrodes varies in terms of speed.[38] In this work, after the exposed surface of the crystals is corroded, extremely regular and parallel domains can be observed inside the crystals, demonstrating that the single crystals exhibit regular geometric growth patterns and the domains are closely interconnected with each other, which further confirms the two-dimensional growth model of the crystals.[22] The average width of the ferroelectric domains first decreases and then increases with an increase in CuO doping amount, as shown in Fig. 5(a–f). Research studies have shown that the miniaturization of ferroelectric domains is

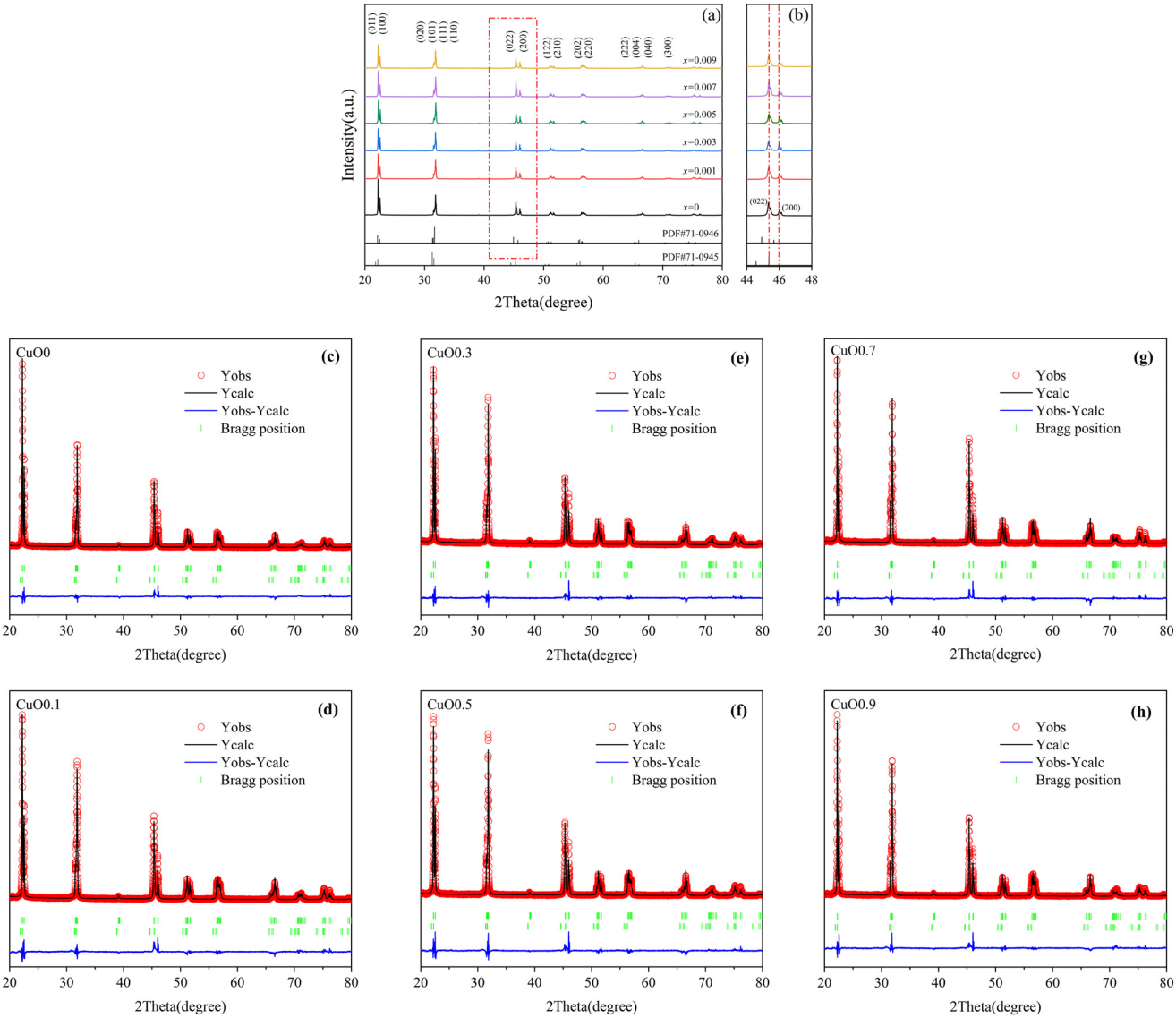

Fig. 3 Powder XRD patterns of (1 − *x*)(KNN-BM)–*x*CuO (*x* = 0, 0.001, 0.003, 0.005, 0.007, 0.009) single crystals. (a) In the 2θ range of 20–80°, (b) enlarged patterns at 2θ = 44–48°, and (c–h) Rietveld refinement results of the XRD data.

Table 1 Rietveld refinement results on the XRD data of CuO-doped 0.996KNN–0.004BM single crystals

Samples	Phases	Percent (wt%)	*a* (Å)	*b* (Å)	*c* (Å)	R_{wp} (%)	χ^2
CuO0	Orthorhombic	99.48	3.94055	5.63346	5.66614	13.3	5.36
	Tetragonal	0.52	3.99751	3.99751	4.06908		
CuO0.1	Orthorhombic	99.11	3.94325	5.63688	5.66880	13.6	5.39
	Tetragonal	0.89	3.99555	3.99555	4.07844		
CuO0.3	Orthorhombic	95.44	3.94404	5.63825	5.67090	12.5	3.82
	Tetragonal	4.56	3.97687	3.97687	4.08562		
CuO0.5	Orthorhombic	94.11	3.94473	5.63894	5.67084	12.8	4.64
	Tetragonal	5.89	3.97537	3.97537	4.09015		
CuO0.7	Orthorhombic	97.62	3.94136	5.63397	5.66665	14.1	5.37
	Tetragonal	2.38	3.99605	3.99605	4.08544		
CuO0.9	Orthorhombic	97.84	3.94219	5.63522	5.66834	13.7	4.47
	Tetragonal	2.16	3.99689	3.99689	4.07553		

beneficial for the activation and deflection of domains,[39–41] thereby improving the piezoelectric properties of crystals.[42] In this case, the variation in the average domain width can be observed in Fig. 5(a and b), as Cu^{2+} ions are introduced,

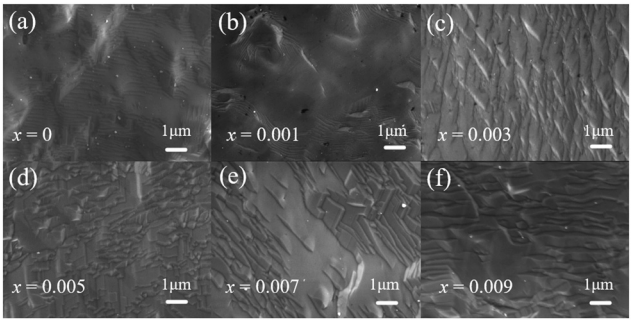

Fig. 4 Natural-surface SEM micrographs of (1 − *x*)(KNN-BM)–*x*CuO single crystals. (a) *x* = 0, (b) *x* = 0.001, (c) *x* = 0.003, (d) *x* = 0.005, (e) *x* = 0.007, and (f) *x* = 0.009.

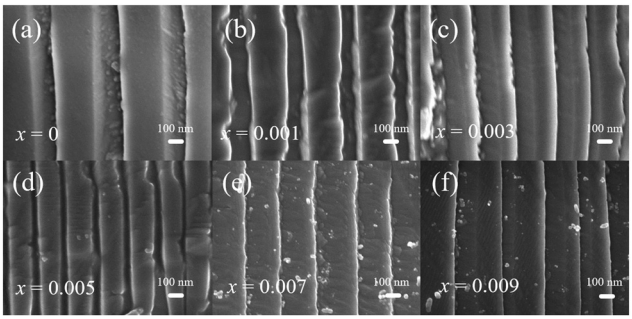

Fig. 5 Cross-section SEM micrographs after corrosion of (1 − *x*)(KNN-BM)–*x*CuO single crystals. (a) *x* = 0, (b) *x* = 0.001, (c) *x* = 0.003, (d) *x* = 0.005, (e) *x* = 0.007, and (f) *x* = 0.009.

the density increases and the defect density decreases for the samples. Moreover, lattice distortion also induces alterations in the internal crystal structure, which is reflected in changes of the domain width,[33,43] the minimum average domain width is 276 nm at *x* = 0.005 for the crystals. As will be mentioned later, this coincides with the optimal piezoelectric coefficient obtained for this crystal at *x* = 0.005. What's more, the pore-free microstructure inside the crystals further proves their high compactness and quality, which would be also conducive to enhancement of piezoelectricity of crystals.

Fig. 6 shows the SEM-EDS plane-scanning maps of the CuO-doped (1 − *x*)(KNN-BM)–*x*CuO crystal for *x* = 0.005, implying that all doped Cu atoms have been uniformly incorporated into the lattices of the crystal. The chemical

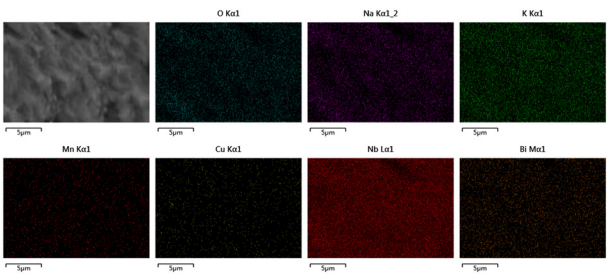

Fig. 6 SEM-EDS plane scanning maps of (1 − *x*)(KNN-BM)–*x*CuO (*x* = 0.005) single crystals.

composition of all the crystals was analyzed by EDS, and the calculated atomic percentages of the elements in the crystal samples are shown in Table 2. It can be found that the atomic ratio for the A-site elements (K, Na), B-site elements (Nb) and oxygen elements is nearly 1 : 1 : 3, which conforms to the stable perovskite ABO_3 structure of the crystals. Of course, due to the inevitable volatilization of alkali metal elements under high temperature conditions, A-site elements (K, Na) have a certain amount of loss, which would lead to the formation of electrical defects such as vacancies in the crystal, thereby increasing the dielectric loss of the crystal. Although the addition of CuO does not play a positive role in preventing the volatilization of A-site elements (K, Na), the introduction of Cu^{2+} ions to some extent neutralizes or balances electrical defects in the crystal, thereby reducing the dielectric loss of the crystal and increasing its piezoelectric and dielectric properties. For example, compared with the undoped CuO, the domain width, leakage effect, dielectric loss and coercive field of the CuO0.1 crystal are reduced to a certain extent, and the piezoelectric properties, dielectric loss, and remanent polarization are improved, as further discussed in the corresponding sections below.

The dependence of the dielectric constant and loss at 50 kHz on temperature for the CuO-doped KNN-BM single crystals is shown in Fig. 7(a–d). As shown in Fig. 7(a), there are two abnormal mutation peaks in the dielectric constant *versus* temperature curves for all the crystals. These two peaks exactly correspond to the transition temperatures from the orthorhombic to tetragonal (T_{O-T}) phase and from the tetragonal to cubic (T_C, Curie temperature) phase. When the CuO-doping amount is *x* = 0.005, the Curie temperature of the sample is 409 °C. The relationship between the transition temperature of these two phases and the CuO-doping amount is shown in Fig. 7(d). With the increase of CuO content, both T_{O-T} and T_C of the crystals change slightly, further indicating no significant change in the crystalline structure of the single crystals after doping, which coincides with the previous crystal structure analysis. According to the crystalline structure, phase content and lattice parameters of the crystals shown in Fig. 3 and Table 1, the structure of the crystals does not show significant changes with the doping amount. Therefore, the Curie temperature of the crystals does not vary significantly with the doping amount of CuO. This is also similar to the results reported by Lin *et al.*[31,44] For ferroelectrics, the changes of the dielectric constant near the Curie temperature follow the Uchino–Nomura equation:[45]

$$\frac{1}{\varepsilon_r} - \frac{1}{\varepsilon_{r,max}} = \frac{(T - T_{max})^{\gamma}}{C}$$

where T_{max} denotes the Curie temperature, $\varepsilon_{r,max}$ is the dielectric constant at Curie temperature, C is a constant and dispersion factor γ = 1 for a classical Curie–Weiss ferroelectric, $1 < \gamma < 2$ for systems showing intermediate degrees of diffuseness, and γ = 2 for a system with a

Table 2 Chemical composition of (1 − *x*)(KNN-BM)–*x*CuO crystals

Samples	Elements (at%)							K/Na ratio	Atomic ratio of A, B and O site elements in ABO_3
	K	Na	Nb	O	Bi	Mn	Cu		
CuO0	9.73	10.61	21.93	57.71	0.05	0.02	0.00	0.91	1.00 : 1.07 : 2.83
CuO0.1	9.49	10.47	22.52	57.49	0.05	0.03	0.01	0.90	1.00 : 1.12 : 2.88
CuO0.3	8.95	10.36	20.89	59.91	0.04	0.01	0.03	0.86	1.00 : 1.08 : 3.10
CuO0.5	9.23	10.50	20.78	59.32	0.06	0.02	0.04	0.88	1.00 : 1.05 : 3.00
CuO0.7	9.64	10.81	22.51	57.10	0.03	0.04	0.06	0.89	1.00 : 1.10 : 2.79
CuO0.9	8.87	10.79	22.33	58.29	0.05	0.02	0.08	0.82	1.00 : 1.13 : 2.96

completely diffused transition.[46] In order to further confirm the relaxation characteristics of KNN, $\ln(T - T_{max})$ is mapped with $\ln(\varepsilon_r^{-1} - \varepsilon_{r,max}^{-1})$, and the slope of the line is the factor γ that characterizes the dispersion degree of the phase transition. Experimental results and fitting results are shown in Fig. 7(b). The fitting results show that the γ value of the KNN single crystal is 1.00, indicating that it is a normal ferroelectric and has no obvious relaxation characteristics.

As can be seen in the inset in Fig. 7(c), the dielectric loss of the undoped sample is relatively high below 100 °C. However, the dielectric loss of the doped crystals is significantly reduced. At x = 0.005, the room-temperature dielectric loss of (1 − x)(KNN-BM)–xCuO is reduced to 0.013, indicating that an appropriate amount of CuO doping can improve the crystal quality and inhibit electrical defects such as oxygen vacancies in the crystals. This supports the above suggestions that the introduction of Cu^{2+} ions neutralized or balanced electrical defects in the crystals, thereby reducing their dielectric loss. In addition, some studies have shown that the doping of CuO would change the lattice parameters which would cause a certain degree of lattice distortion, and reduce the DC leakage current and activation energy of materials, which would also lead to changes in dielectric loss.[47]

Fig. 8(a) shows the polarization *versus* electrical field (*P*–*E*) loops of the (1 − x)(KNN-BM)–xCuO single crystals under an electric field of 30 kV cm^{-1}. All single crystal samples exhibit typical ferroelectric properties with similar *P*–*E* loops. Fig. 8(b) shows the dependence of the remanent polarization (P_r) and coercive field (E_c) on the CuO doping content of the crystals. It can be clearly seen that the P_r value of the single crystal samples is in the range of 20–35 μC cm^{-2}, and the E_c value is 9.5–13.0 kV cm^{-1}. On the whole, after doping, the remanent polarization of the crystals was enhanced while the coercive field was reduced. These are attributed to the facts that the variation in the average width of the domains and lattice distortion induced by the addition of Cu^{2+} ions facilitate the activation of ferroelectric domains in the crystals, which strengthens the polarization of the crystals. However, excessive CuO doping leads to a slight increase in the coercive field due to the pinning effect that hinders domain rotation to some extent.[8] For ferroelectric materials, if in a view from the relationship between domain size and ferroelectricity, in general, fine domains do correspond to low coercive fields. However, aside from the size of the domain, there are other factors that affect the coercive field of ferroelectric materials, such as the defect pinning effect. According to the previous results, it can be seen that the addition of CuO can not only reduce the size of domains, but it also introduces electrochemical defects. Excessive addition of CuO introduces a large number of defects, which would produce a strong pinning effect on domain rotation, which would be superior to the domain rotation promotion effect caused by domain refinement. That's the reason why the smallest E_c appears in the CuO0.1 sample, while the smallest domain size sample is CuO0.5.

Fig. 8(c) shows the d_{33} value of the (1 − x)(KNN-BM)–xCuO single crystals as a function of CuO content. As can be seen in Fig. 8(c), the CuO-doping content has a great influence on the value of d_{33}. It first increases and then decreases with addition of CuO, with the maximum value of 314 pC N^{-1} for the crystal at x = 0.005, which corresponds to the optimization of the crystalline defects and domain structure caused by CuO doping in the crystals, as mentioned above. This result corresponds to the substitution of copper ions for B site ions mentioned above, which affects the piezoelectric effect of the system.[48,49] Fig. 8(c) also shows the relationship between the mechanical quality factor (Q_m), the electromechanical coupling coefficient (K_t) and the CuO content (x) for the (1 − x)(KNN-BM)–xCuO single crystals. The variation of these two parameters with x is similar to that of d_{33} with x for the crystals. This also manifests that Cu doping together with Bi and Mn can effectively enhance the piezoelectric and ferroelectric properties of KNN crystals by optimizing their structure.

In order to study the origins of enhanced piezoelectric and ferroelectric properties in the copper-doped KNN single crystals, the leakage current density of the copper-doped and undoped KNN crystals was measured (Fig. 8d). The KNN single crystal doped with an appropriate amount of CuO shows a lower leakage current density ($<3 \times 10^{-5}$ A cm^{-2}) than the undoped KNN single crystal. Generally, the leakage current mechanisms include interface-confined Schottky emission (SE), bulk-confined Poole–Frenkel emission (PFE) and space-charge-limited current (SCLC).[50] In order to study the leakage mechanism of the crystals, Fig. 8(e) shows the $\ln J$–$\ln E$ curves of the KNN single crystals. All samples have a linear relationship between $\ln J$ and $\ln E$ in a low electric field ($\ln E <$ 12.5 V m^{-1}). For the undoped and 0.7 at% CuO KNN single crystals, the linear fitting slope of the curves is 1.9397 and 2.3271 Ω^{-1} m^{-1}, respectively. In general, when the slope is close

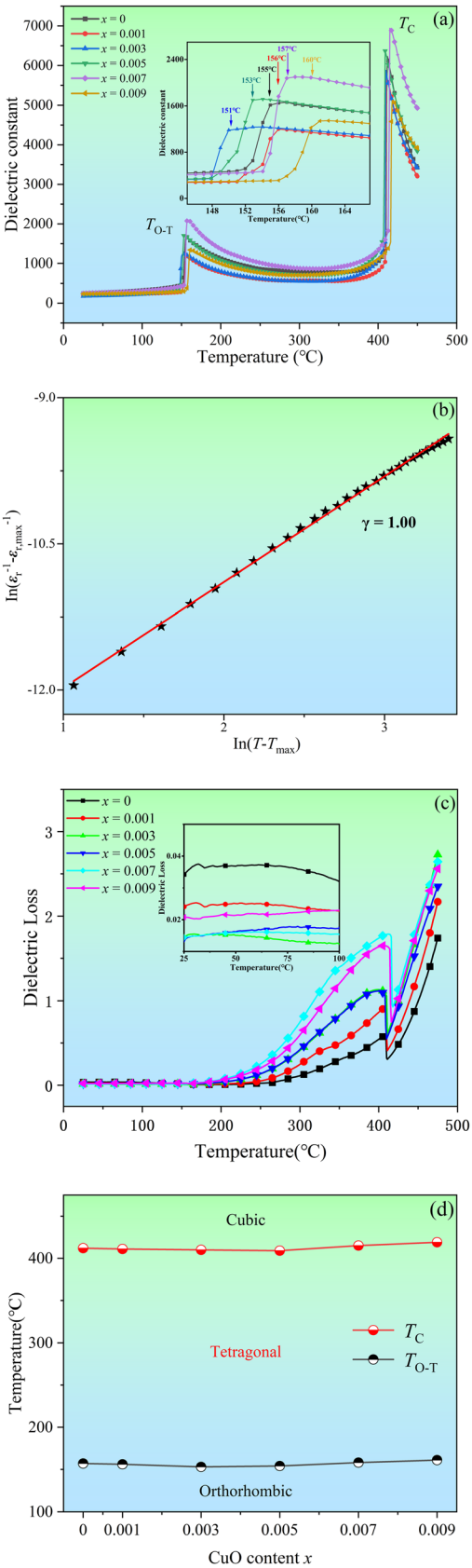

Fig. 7 Dielectric properties of the (1 − *x*)(KNN-BM)–*x*CuO crystals. (a) The curves of dielectric permittivity *versus* temperature, (b) relaxation characteristic fitting results, (c) the curves of dielectric loss *versus* temperature, and (d) the relationship of T_C and T_{O-T} *versus* *x*.

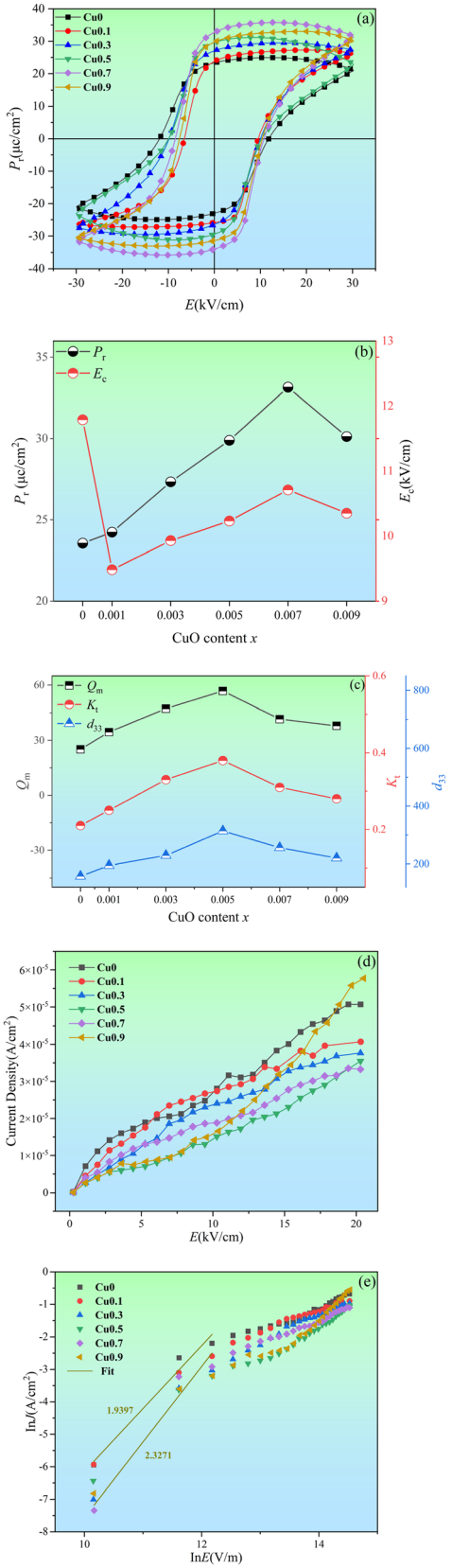

Fig. 8 Ferroelectric and piezoelectric properties and leakage spectra of (1 − *x*)(KNN-BM)–*x*CuO crystals. (a) *P*–*E* loops, (b) relationship between the remnant polarization P_r, coercive field E_c and CuO content *x*, (c) the dependence of d_{33}, Q_m, and K_t on the *x*, (d) leakage current density *versus* electric field (*J*–*E*), and (e) curves of ln *J*–ln *E*.

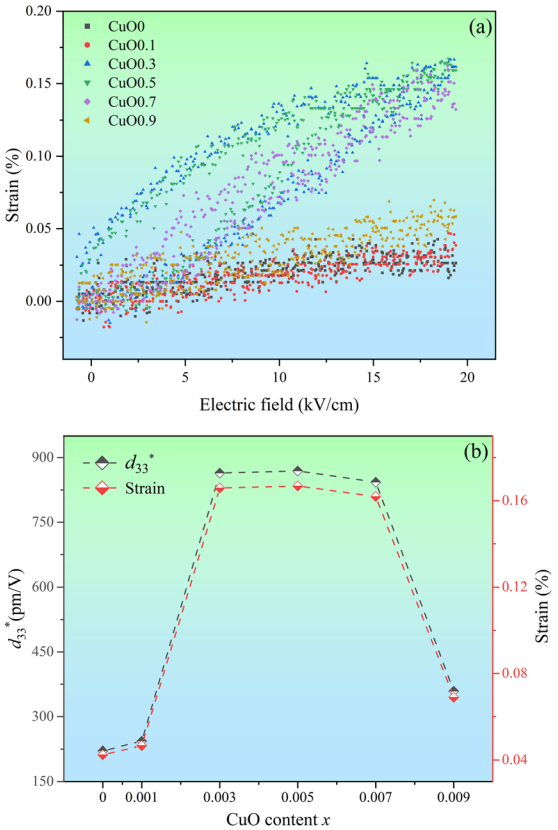

Fig. 9 The (a) unipolar *S*–*E* loops at 1 Hz and (b) strain and inverse piezoelectric coefficient (d_{33}^*) *versus* CuO content (*x*) relationship for (1 − *x*)(KNN-BM)–*x*CuO crystals.

to 2 or greater than 2, the conduction belongs to the SCLC conduction mechanism,[51] indicating that in a low electric field ($\ln E < 12.5$ V m^{-1}), the conduction in the crystals is the SCLC mechanism. Kizaki Noguchi *et al.* attributed the high *J* of KNN-based crystals to the electrical conduction through 4d electrons of Nb, and ion vacancies generated by volatile substances (such as K, Na and Bi in the KNN crystals).[52] An appropriate amount of CuO doping as a buffer material inhibits the generation of vacancies, and copper ions preferentially occupy the Nb(B) sites, resulting in a decrease in the leakage current.[9] Similarly, the decrease of leakage current caused by an appropriate amount of CuO doping can also prove the decrease of dielectric loss in the crystals.

Fig. 9(a) shows the electric field–strain curves of the (1 − *x*)(KNN-BM)–*x*CuO single crystals measured at a frequency of 1 Hz. The results can be found from Fig. 9(b) that with the increase of CuO-doping content, the unipolar strain and inverse piezoelectric coefficient of the single crystals first increase and then decrease gradually under the same electric field conditions. Under the electric field of 20 kV cm^{-1}, when x = 0.005, the single crystal obtains the highest strain value S_{max} of 0.16%. At this moment, the calculated inverse piezoelectric coefficient (d_{33}^*) of the crystal reaches 869 pm V^{-1}. This demonstrates that the addition of a small amount of CuO may also increase the inverse piezoelectric coefficient and electrostriction of the crystals. In general, the inverse piezoelectric effect of piezoelectric materials is closely related to their piezoelectric coefficient. For example, Duong[53] and Liu[54] *et al.* reported that the samples with the highest piezoelectric coefficient also had the highest inverse piezoelectric coefficient for some doped or textured KNN-based ceramics.

Table 3 lists some parameters of the main electrical properties for the crystals in the present work. For comparison, Table 3 also includes the parameters for the KNN ceramics and crystals reported in the literature. Compared with the results reported by the references, the crystals in this work show higher positive and inverse piezoelectric constants and remanent polarization intensity as well as smaller dielectric loss and coercive field by introducing Cu, Bi and Mn elements together. At the same time, the seed-free solid state crystal growth method used in this work has some advantages, such as easier operation, lower energy consumption and cost, better composition homogeneity, and so on. Moreover, the internal domain structure and leakage current density of the crystals were also studied and reported in this work. These results show that the Cu, Bi and Mn co-doped KNN crystals grown by the SFSSCG method have broad prospects in future practical applications.

Conclusions

In the present study, lead-free piezoelectric (1 − *x*)(0.996$K_{0.5}$-$Na_{0.5}NbO_3$–0.004$BiMnO_3$)–*x*CuO (*x* = 0–0.009) single crystals

Table 3 Comparison of electrical properties of the CuO-doped KNN-BM crystals and other KNN-based ceramics and crystals reported previously

Materials	d_{33} (pC N^{-1})	P_r (μC cm^{-2})	tan δ	T_c (°C)	K_t (%)	d_{33}^* (pm V^{-1})	E_c (kV cm^{-1})	Ref.
KNN-MB–0.5% CuO[a]	314	33.2	0.013	409	38	869	9.48	This work
KNN[a]	110	20	<0.05	~400	45	—	20	55
KNN–MnO_2[a]	261	22.06	0.015	412	65.9	—	17.93	56
KNN–Li[a]	255	26.1	0.01	415	—	313	<10	12
KNN25/75[a]	145	—	—	396	69	—	—	19
KNN-TL[a]	354	—	—	—	—	672	—	57
KNN–$BaTiO_3$[b]	104	7.5	0.038	358	39	—	12	58
KNN–$CaTiO_3$[b]	115	12.4	—	410	42.1	—	12.2	59
KNN–CuO[b]	146	—	0.016	415	58	—	—	60
KNN–$SrZrO_3$[b]	256	~22	0.026	353	46	<500	—	61

[a] Single crystals. [b] Ceramics.

were prepared using the SFSSCG method with $BiMnO_3$ and CuO as dopants. Subsequently, the effects of the CuO doping concentration on the morphology, crystal structure and electrical properties of the KNN-BM crystals were systematically studied. It was found that an appropriate amount of CuO doping can promote the growth of the crystals and enhance their electrical properties. When the diameters of the billets were 25 and 40 mm, the maximum crystal sizes of 19 × 17 × 2 and 25 × 21 × 2 mm^3 were obtained. All crystals were compact, with almost no holes, and had an orthorhombic-dominated perovskite structure. The crystals were normal ferroelectrics and had no relaxation characteristics. The smallest average domain width was found in the crystal at $x = 0.005$, whose leakage current density was less than 3×10^{-5} cm^2 in a low electric field ($\ln E < 12.5$ V m^{-1}). In a low electric field ($\ln E < 12.5$ V m^{-1}), the conduction in the crystal was the space-charge-limited current (SCLC) mechanism. Meanwhile, the crystal obtained the largest piezoelectric constant and other excellent electrical properties: d_{33} = 314 pC N^{-1}, P_r = 29.9 μC cm^{-2}, E_c = 10.1 kV cm^{-1}, Q_m = 56.8, K_t = 0.38, d_{33}^* = 869 pm V^{-1}, T_C = 409 °C, and $\tan\delta$ = 0.013. These results show that the CuO-doped KNN-BM crystals would have broad application prospects in the future.

Data availability

All relevant data are within the paper. The data are available from the corresponding author on reasonable request.

Author contributions

Yuan Xu: writing – original draft, investigation, formal analysis. Minhong Jiang: supervision, conceptualization, writing – review & editing, investigation, funding acquisition, methodology. Xinkang Liu, Yujiao Zeng, Shixuan Cao, Yujiao Ouyang, and Jianwei Song: methodology, investigation, formal analysis. Guanghui Rao: methodology, resources, funding acquisition.

Conflicts of interest

The authors declare that they have no known competing financial interests or personal relationships that could have appeared to influence the work reported in this paper.

Acknowledgements

This work was supported by the National Natural Science Foundation of China (52172001), the Guangxi Natural Science Foundation (2022GXNSFDA035082), the Guangxi Key Laboratory of Information Materials (Guilin University of Electronic Technology, Project No. 211006-Z) and the Program for Bagui Scholars of Guangxi.

References

1 Y. Saito, H. Takao, T. Tani, T. Nonoyama, K. Takatori, T. Homma, T. Nagaya and M. Nakamura, *Nature*, 2004, **432**, 84–87.
2 A. Rahman, M. Jiang, G. Rao, S. Lee, M.-H. Kim, M. Habib and J. U. Rahman, *Ceram. Int.*, 2022, **48**, 20251–20259.
3 C.-W. Ahn, H.-Y. Lee, G. Han, S. Zhang, S.-Y. Choi, J.-J. Choi, J.-W. Kim, W.-H. Yoon, J.-H. Choi, D.-S. Park, B.-D. Hahn and J. Ryu, *Sci. Rep.*, 2015, **5**, 17656.
4 L. Peng, X. Gao, X. Liu and M. Jiang, *Mater. Today Commun.*, 2024, **38**, 108214.
5 T. Wang, M. Jiang, L. Li, S. Cheng, H. Lu, P. Ren, Y. Zhao and G. Rao, *J. Alloys Compd.*, 2023, **935**, 168126.
6 Y. Zhao, M. Jiang, L. Li, T. Wang, P. Ren and G. Rao, *J. Mater. Sci.: Mater. Electron.*, 2023, **34**, 689.
7 P. Ren, M. Jiang, H. Lu, L. Li, S. Cheng, T. Wang, Y. Zhao and G. Rao, *J. Mater. Sci.: Mater. Electron.*, 2023, **34**, 465.
8 H. Lu, M. Jiang, X. Yao, Z. Zhang, W. Wang, L. Li and G. Rao, *J. Mater. Sci.: Mater. Electron.*, 2022, **33**, 2816–2828.
9 X. Yao, M. Jiang, S. Han, D. Li, Y. Xu, L. Li and G. Rao, *J. Mater. Res.*, 2021, **36**, 1182–1194.
10 A. Cui, X. Cao, Y. Ye, K. Jiang, L. Zhu, M. Jiang, G. Rao, Y. Li, Z. Hu and J. Chu, *Phys. Rev. B*, 2020, **102**, 214102.
11 X. Yao, M. Jiang, W. Li, H. Lu, L. Li and G. Rao, *J. Mater. Sci.: Mater. Electron.*, 2020, **31**, 21971–21980.
12 D. Li, M. Jiang, S. Han, Q. Jin, Y. Xu, X. Yao, K. Zhang, L. Li, L. Miao, C. Zhou and G. Rao, *J. Mater. Sci.: Mater. Electron.*, 2020, **31**, 4857–4866.
13 M. Jiang, J. Zhang, G. Rao, D. Li, C. A. Randall, T. Li, B. Peng, L. Li, Z. Gu, X. Liu and H. Huang, *J. Mater. Chem. C*, 2019, **7**, 14845–14854.
14 B.-J. Chu, D.-R. Chen, G.-R. Li and Q.-R. Yin, *J. Eur. Ceram. Soc.*, 2002, **22**, 2115–2121.
15 Q. Zhang, X. Zhao, R. Sun and H. Luo, *Phys. Status Solidi A*, 2011, **208**, 1012–1020.
16 J. Koruza, H. Liu, M. Höfling, M.-H. Zhang and P. Veber, *J. Mater. Res.*, 2020, **35**, 990–1016.
17 X. Huo, L. Zheng, S. Zhang, R. Zhang, G. Liu, R. Wang, B. Yang, W. Cao and T. R. Shrout, *Phys. Status Solidi RRL*, 2013, **8**, 86–90.
18 H. Zhou, H. Deng, X. Liu, H. Yan, X. Zhao, H. Luo and J. Xu, *Ceram. Int.*, 2016, **42**, 15327–15331.
19 H. Deng, X. Zhao, H. Zhang, C. Chen, X. Li, D. Lin, B. Ren, J. Jiao and H. Luo, *CrystEngComm*, 2014, **16**, 2760–2765.
20 M. Jiang, S. Han, J. Zhang, J. Song, C. Hao, M. Deng, L. Ge, Z. Gu and X. Liu, *J. Cryst. Growth*, 2018, **483**, 258–264.
21 J. Song, C. Hao, Y. Yan, J. Zhang, L. Li and M. Jiang, *Mater. Lett.*, 2017, **204**, 19–22.
22 C. Y. Hao, Z. F. Gu, G. Cheng, L. Li, J. W. Zhang, J. G. Song, Y. F. Yan and M. H. Jiang, *J. Mater. Sci.: Mater. Electron.*, 2017, **28**, 18357–18365.
23 M. Jiang, C. A. Randall, H. Guo, G. Rao, R. Tu, Z. Gu, G. Cheng, X. Liu, J. Zhang, Y. Li and G. Brennecka, *J. Am. Ceram. Soc.*, 2015, **98**, 2988–2996.
24 Z. Guangqian, J. Minhong, M. Jiafeng, P. Ling and Z. Jinwei, *J. Mater. Sci.: Mater. Electron.*, 2015, **26**, 6434–6438.
25 M. H. Jiang, G. Q. Zhao, Z. F. Gu, G. Cheng, X. Y. Liu, L. Li and Y. S. Du, *J. Mater. Sci.: Mater. Electron.*, 2015, **26**, 9366–9372.

26 P. Ling, J. Minhong, G. Zhengfei, C. Gang, M. Lei, D. Yusong, W. Xiaofei, R. Guanghui and L. Yongxiang, *J. Mater. Sci.: Mater. Electron.*, 2013, **25**, 323–327.
27 A. Rahman, M. Jiang, G. Rao, S. Lee, M.-H. Kim, M. Habib and J. U. Rahman, *Ceram. Int.*, 2022, **48**, 20251–20259.
28 J. Yang, F. Zhang, Q. Yang, Z. Liu, Y. Li, Y. Liu and Q. Zhang, *Appl. Phys. Lett.*, 2016, **108**, 182904.
29 X. Peng, B. Zhang, L. Zhu, L. Zhao, R. Ma, B. Liu and X. Wang, *J. Adv. Ceram.*, 2018, **7**, 79–87.
30 T. Wang, D. Wang, Y. Liao, Q. Zheng, H. Sun, K. W. Kwok, N. Jiang, W. Jie, C. Xu and D. Lin, *J. Eur. Ceram. Soc.*, 2018, **38**, 4915–4921.
31 D. Lin, K. W. Kwok and H. L. W. Chan, *Appl. Phys. Lett.*, 2007, **90**, 232903.
32 Z.-Y. Shen, Y. Xu and J.-F. Li, *Ceram. Int.*, 2012, **38**, S331–S334.
33 J.-J. Zhou, L.-Q. Cheng, K. Wang, X.-W. Zhang, J.-F. Li, H. Liu and J.-Z. Fang, *Ceram. Int.*, 2014, **40**, 2927–2931.
34 X. Liu, M. Jiang, Y. Zeng, Y. Ouyang, Y. Xu, S. Cao, J. Song, L. Li, S. Cheng and G. Rao, *J. Mater. Sci.: Mater. Electron.*, 2024, **35**, 780.
35 C. Medrano, M. Zgonik, I. Liakatas and P. Günter, *J. Opt. Soc. Am. B*, 1996, **13**, 2657–2661.
36 Y. Shen and Z. Zhou, *Chem. Phys. Lett.*, 2008, **454**, 114–117.
37 J. Song, C. Hao, Y. Yan, J. Zhang, L. Li and M. Jiang, *Mater. Lett.*, 2017, **204**, 19–22.
38 R. Lopez-Sesenes, I. Rosales, J. Uruchurtu-Chavarin, V. M. Salinas-Bravo and J. G. González-Rodriguez, *Int. J. Electrochem. Sci.*, 2018, **13**, 4827–4840.
39 W.-Y. Chang, C.-C. Chung, C. Luo, T. Kim, Y. Yamashita, J. L. Jones and X. Jiang, *Mater. Res. Lett.*, 2018, **6**, 537–544.
40 J. Xu, H. Deng, Z. Zeng, Z. Zhang, K. Zhao, J. Chen, N. Nakamori, F. Wang, J. Ma, X. Li and H. Luo, *Appl. Phys. Lett.*, 2018, **112**, 182901.
41 J. Xiong, Z. Wang, X. Yang, R. Su, X. Long and C. He, *RSC Adv.*, 2021, **11**, 12826–12832.
42 L. M. Eng, *Nanotechnology*, 1999, **10**, 405–411.
43 S. Kar and K. S. Bartwal, *Cryst. Res. Technol.*, 2008, **43**, 679–682.
44 D. Lin, K. W. Kwok and H. L. W. Chan, *J. Phys. D: Appl. Phys.*, 2008, **41**, 045401.
45 K. Uchino and S. Nomura, *Ferroelectrics*, 2011, **44**, 55–61.
46 C. Wang, J. Chen, L. Shen, J. Rui, X. Yang, M. Zhu and Y. Hou, *J. Ceram. Sci. Technol.*, 2017, **8**, 255–258.
47 S. Singhal, J. Kaur, T. Namgyal and R. Sharma, *Phys. B*, 2012, **407**, 1223–1226.
48 G. Jiao, H. Fan, L. Liu and W. Wang, *Mater. Lett.*, 2007, **61**, 4185–4187.
49 F. Zhang, S. Fan, Y. Zhu, W. Chen, B. Liu, Y. Yang, L. Zheng, Y. Zhang, X. Lv and X. Wang, *J. Materiomics*, 2024, **10**, 1017–1025.
50 L. Wang, W. Ren, P. Shi and X. Wu, *J. Appl. Phys.*, 2014, **115**, 034103.
51 P. M. Raj, B.-W. Lee, D. Balaraman and R. R. Tummala, *J. Electroceram.*, 2011, **27**, 169–175.
52 Y. Kizaki, Y. Noguchi and M. Miyayama, *Appl. Phys. Lett.*, 2006, **89**, 142910.
53 T. A. Duong, C. W. Ahn, B. W. Kim, M. R. Bafandeh, H.-S. Han and J.-S. Lee, *J. Electron. Mater.*, 2022, **51**, 1490–1497.
54 Z. Liu, Q. Zhang, W. Cai, G. Chen, X. Li, R. Gao, X. Deng and C. Fu, *Mater. Lett.*, 2023, **351**, 135098.
55 M. A. Rafiq, M. E. V. Costa and P. M. Vilarinho, *Sci. Adv. Mater.*, 2014, **6**, 426–433.
56 H. Zhou, H. Deng, X. Liu, H. Yan, X. Zhao, H. Luo and J. Xu, *Ceram. Int.*, 2016, **42**, 15327–15331.
57 X. Huo, L. Zheng, R. Zhang, R. Wang, J. Wang, S. Sang, Y. Wang, B. Yang and W. Cao, *CrystEngComm*, 2014, **16**, 9828–9833.
58 Y. Guo, K.-i. Kakimoto and H. Ohsato, *Jpn. J. Appl. Phys.*, 2004, **43**, 6662–6666.
59 R.-C. Chang, S.-Y. Chu, Y.-F. Lin, C.-S. Hong, P.-C. Kao and C.-H. Lu, *Sens. Actuators, A*, 2007, **138**, 355–360.
60 Y. Chang, S. F. Poterala, Z. Yang, S. Trolier-McKinstry and G. L. Messing, *J. Mater. Res.*, 2011, **25**, 687–694.
61 J. Zhou, G. Xiang, J. Shen, H. Zhang, Z. Xu, H. Li, P. Ma and W. Chen, *J. Electroceram.*, 2019, **44**, 95–103.